Functional Complex Point-Defect Structure in a Huge-Size-Mismatch System

Ryo Ishikawa,[1] Naoya Shibata,[1,2] Fumiyasu Oba,[3] Takashi Taniguchi,[4]
Scott D. Findlay,[5] Isao Tanaka,[3,6] and Yuichi Ikuhara[1,6,7,*]

[1]*Institute of Engineering Innovation, University of Tokyo, 2-11-16, Yayoi, Bunkyo, Tokyo 113-8656, Japan*

[2]*Japan Science and Technology Agency, Precursory Research for Embryonic Science and Technology (PRESTO),
Kawaguchi, Saitama 332-0012, Japan*

[3]*Department of Materials Science and Engineering, Kyoto University, Sakyo, Kyoto 606-8501, Japan*

[4]*Advanced Key Technologies Division, National Institute for Materials Science, 1-1 Namiki, Tsukuba, Ibaraki 305-0044, Japan*

[5]*School of Physics, Monash University, Victoria 3800, Australia*

[6]*Nanostructures Research Laboratory, Japan Fine Ceramics Center, 2-4-1 Mutsuno, Atsuta, Nagoya 456-8587, Japan*

[7]*World Premier International Research Center, Advanced Institute for Materials Research, Tohoku University,
2-1-1 Katahira, Aoba-ku, Sendai 980-8577, Japan*

Cubic boron nitride is a promising system for photonics and optoelectronics. Determining the inclusion mechanisms for dopants with a large size mismatch, such as luminous rare-earth elements, is prerequisite to understanding their functional properties and to effective doping control. Combining evidence from subangstrom resolution scanning transmission electron microscopy, imaging simulations, and first-principles calculations, we show that cationic Ce^{3+} single dopants are not located at cationic B sites but rather at anionic N sites surrounded by B-site vacancies.

PACS numbers: 61.72.J−, 68.37.Ma, 78.60.Hk, 79.20.Uv

Cubic boron nitride (*c*-BN) is the next hardest material after diamond and is used in many mechanical applications due to its excellent hardness and chemical stability [1]. *c*-BN is also well known as the lightest III–V semiconductor. With the large band gap of $E_g = 6.2$ eV [1], it is attractive as a host material in various optoelectronic applications such as photoemitters, scintillators, lasers, and light-emitting diodes in the UV or visible range [2]. For *c*-BN to realize its full potential, impurity control and effective doping are essential. However, very little is known in this regard. Because of the strong covalent bonding nature and also the small size of the constituent B and N atoms, the elements that can be readily incorporated into *c*-BN are limited to those of relatively light weight and small size: Be, C, O, Si, and S [3–6]. It has been extremely difficult to introduce luminous dopants such as rare-earth (R) elements into the *c*-BN lattice because of the huge size mismatch between the host lattice and these dopant atoms. Recently, crystal growth by using reactive flux with the temperature gradient method at high pressure and high temperature (5 GPa, 1500 °C) has achieved stable doping of rare-earth atoms into the *c*-BN host lattice, and we have firstly produced the large-scale (millimeter size) *c*-BN:R single crystals with luminous features [7–9]. To understand the doping mechanism and emergence of luminous properties in materials with strong covalent bonding, the fundamental question remains as to how dopant atoms with a large size mismatch can be accommodated within the host crystal lattices. In the present study, we show the direct determination of the exact atomic sites and valence states of individual rare-earth dopant atoms (Ce) buried inside *c*-BN crystals using atomic-resolution scanning transmission electron microscopy (STEM). Combined with first-principles calculations, we uncover the mechanism for accommodating these large dopant atoms into the host crystalline lattice: the formation of complex point-defect structures. Our results elucidate how *c*-BN with strong covalent bonding nature can accept a dopant with a large size mismatch.

The *c*-BN:Ce single crystals observed in this study were synthesized by the temperature gradient method at 5.5 GPa and 1500 °C for 80 h. In order to efficiently dope Ce atoms, 0.5 wt% of Ce fluoride powder was mixed with a barium boron nitride solvent, and we obtained 0.5 ∼ 1 mm cube single crystals (optically transparent). Figure 1(a) shows a cathodoluminescence optical image of a *c*-BN:Ce single crystal. The blue-colored luminescence, with a broad but single pronounced peak at 430 nm, is assigned to the intrinsic 4*f*-5*d* electron transition of Ce^{3+} atoms buried inside a bulk material [2]. The homogeneous luminescence suggests that the Ce atoms are uniformly doped throughout the whole specimen area. For the preparation of electron-transparent thin TEM specimens, *c*-BN:Ce single crystals were cut out perpendicular to the [110] crystallographic direction and mechanically polished using a diamond suspension, followed by Ar ion beam milling procedures. To minimize surface damage and contamination, Ar ion beam milling was performed at 0.5 kV in the final stage. In the present atomic-scale analysis, we used an aberration-corrected STEM (JEM ARM-200CF, JEOL Ltd.), operated at 200 kV, and both annular dark-field (ADF) and electron energy-loss spectroscopy (EELS) imaging modes. In ADF STEM, the signal intensity depends on the scattering power of the atoms (Z contrast) [10]. ADF STEM is
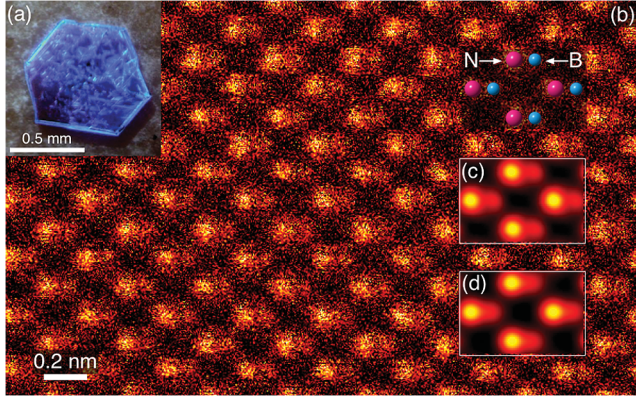
FIG. 1 (color). (a) Blue luminous cathodoluminescence optical image obtained from a c-BN:Ce single crystal. Atomic-resolution ADF STEM images of c-BN viewed along the [110] direction: (b) as recorded and (c) averaged to reduce the scan noise and enhance the visibility (by simple summation of equivalent areas). The structure model (zinc-blende type) is overlaid on (b), with the B and N atoms shown in blue (right) and red (left), respectively. The specimen thickness is determined to be ~12 nm by means of the EELS log-ratio method [28]. (d) Simulated image, obtained under the present microscope conditions: the probe-forming aperture half-angle is 24.5 mrad and the half-angle of the ADF detector spans from 68 to 280 mrad.

therefore well suited to the identification of the atomic site of heavy Ce dopants inside ultralight c-BN crystals ($Z_B = 5$, $Z_N = 7$, $Z_{Ce} = 58$), though clear, simultaneous imaging of the light element supporting matrix as needed to identify the crystallographic sites occupied by the Ce dopants remains challenging. To avoid irradiation damage, atomic-resolution observations were performed under low-dose conditions: the probe current was set below ~8 pA with a cold field-emission gun. Under these conditions, c-BN is remarkably stable and no apparent change can be recognized even after 15 min of probe scanning.

Figure 1(b) shows an atomic-resolution ADF STEM image of c-BN viewed along the [110] direction. Because of the weak scattering strength of the B and N atoms, the image contrast is relatively weak. However, the subangstrom BN dumbbells (the projected spacing is 0.9 Å) are clearly resolved even under our low-dose imaging conditions. Moreover, the B and N atomic columns can be distinguished. This is most evident in the averaged image shown in Fig. 1(c). All these features are well reproduced in the image simulations shown in Fig. 1(d).

Figure 2(a) shows a typical ADF STEM image of c-BN:Ce viewed along the [110] direction. Randomly distributed brighter spots highlight the atomic columns containing Ce atoms. The absolute brightness depends on the location of the Ce atoms along the specimen depth [11–13]. Previous work on imaging heavy dopants in lighter substrates has utilized depth sectioning as a means of maximizing the contrast due to individual dopants [14,15], but here it is necessary to maintain a probe focus such as to

obtain a clear image of the supporting lattice as a reference for the crystallographic positions of the Ce atoms. The atomic-resolution images clearly reveal that the Ce atoms do not form Ce-clusters but are distributed in the c-BN lattice as single atoms. These single Ce atoms contribute equally to the unique blue-colored luminescence. From a statistical analysis of the images, the Ce concentration in the observed volumes can be estimated to be about $(7.2 \pm 1.2) \times 10^{18}$ atoms cm^{-3}, which is comparable to the results of secondary-ion mass spectroscopy: $(2.6 \pm 0.1) \times 10^{18}$ atoms cm^{-3} (see Secs. S1–S3 in the Supplemental Material [16]). In the higher-magnification image shown in Fig. 2(b), all the Ce dopant atoms substitute for the exact N site (Ce$_N$), not for the cationic B site, as is most evident in the Gaussian filtered image and its line profile shown in Figs. 2(c) and 2(d). The brighter feature at the N atomic columns is also reproduced in the simulated image [inset of Fig. 2(b)] based on the $(\text{Ce}_N - 4V_B)^{6-}$ complex point-defect structure, as we discuss presently. Before acquisition of the final ADF STEM images, probe scanning was repeated several times to exclude any possibility of Ce adatoms on the surface (the adatoms move on the surface during the scanning). Thus we confirmed that all the Ce atoms in Fig. 2(b) are stable at the N sites and buried inside the c-BN crystal.

The valence state of the single Ce atoms inside the c-BN crystal was investigated using column-by-column EELS under the same probe conditions as the ADF STEM. Although the background level in the spectrum is relatively high, two distinct peaks at 883 and 901 eV can be identified as the Ce M_5 and M_4 edges, respectively [Fig. 2(e)]. By comparison to the EEL spectra of Ce^{3+} in Ce$_2$O$_3$ and Ce^{4+} in CeO$_2$ [17], the valence state of the Ce atoms is determined to be $3+$. This conclusion was further supported by using the M_4/M_5 ratio with the second derivative spectrum [18]. These features were reproduced for several different Ce atoms. No significant electron irradiation damage was observed after EELS acquisition.

To determine the stable Ce atom configurations in the c-BN lattice, we evaluated the relaxed structure and formation energies of substitutional Ce atoms and their related defect complexes using hybrid Hartree-Fock density functional calculations [19–22]. The calculations were performed using the projector augmented-wave method [23] and the Heyd-Scuseria-Ernzerhof (HSE06) hybrid functional [24] as implemented in the VASP code [25]. Supercells containing 216 atoms and a defect were employed and cell-size corrections were applied using the scheme reported in Ref. [26]. More details on the computational methods can be found in the Supplemental Material [16]. The formation energy (E_f) of a defect is obtained as

$$E_f = E_T^{\text{def}} - \sum_i n_i \mu_i + q \epsilon_F, \quad (1)$$

where E_T^{def} denotes the total energy of the supercell with a defect in charge state q; n_i is the number of the constituent
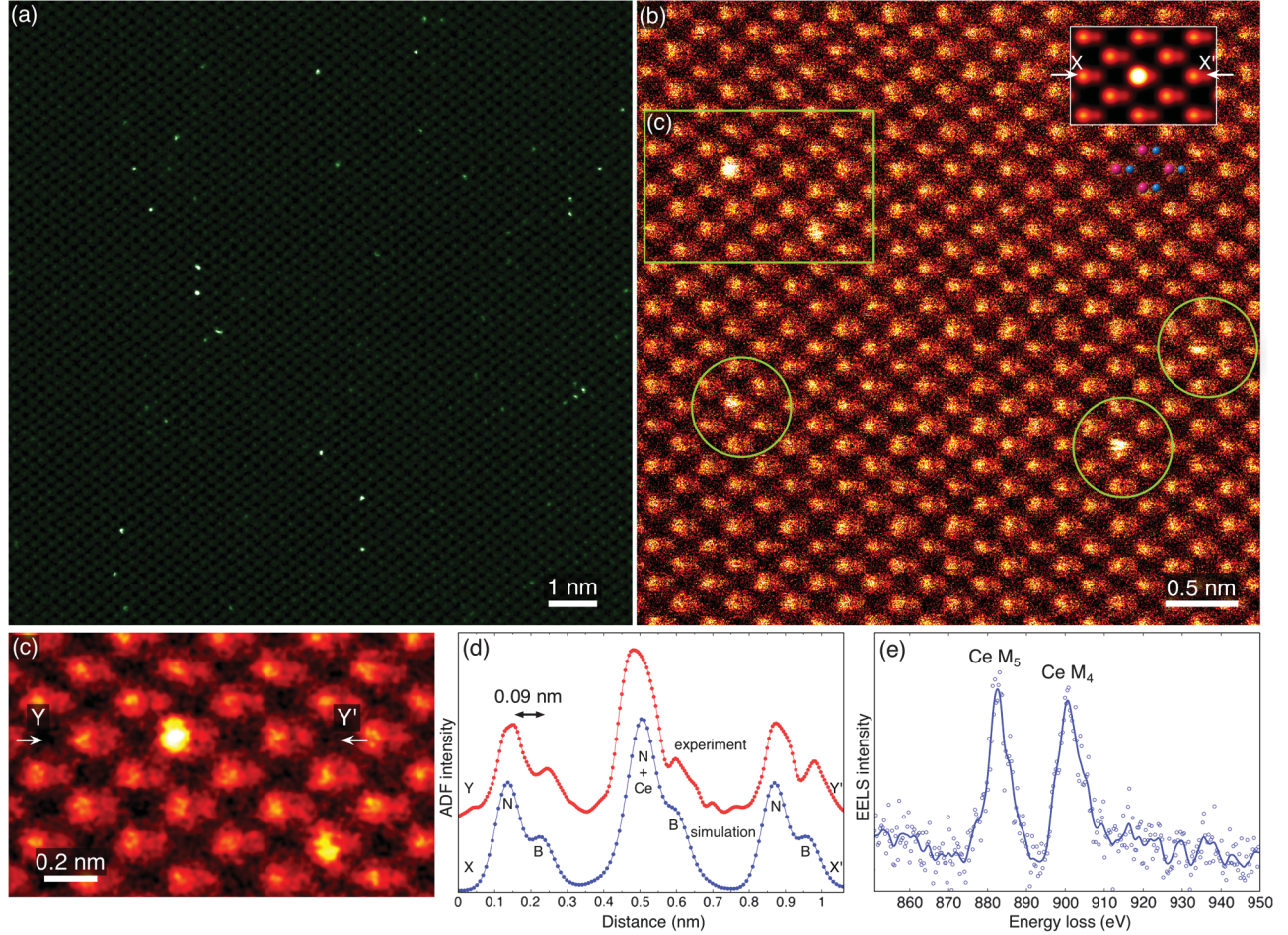
FIG. 2 (color). (a) ADF STEM image of c-BN:Ce viewed along the [110] direction (Gaussian filter is performed). High magnification ADF STEM images: (b) as recorded and (c) Gaussian filtered. The specimen thickness is ~ 14 nm, measured by EELS. (d) Intensity profiles along X–X' and Y–Y' in the simulated [inset of (b)] and experimental (c) images, respectively. The image simulation is based on the $(Ce_N$-$4V_B)^{6-}$ complex point-defect structure [see Figs. 3(c)–3(e)], and the Ce atom is assumed to be at a depth of 5 nm in the 14 nm thick specimen. The experimental intensity profile is well reproduced by the simulation. (e) Core-loss spectrum obtained from a single nitrogen atom column containing one Ce atom. The peaks are identified as the Ce M_5 and M_4 edges, respectively.

atoms of i type; μ_i and ϵ_F are the atomic chemical potential and the Fermi level. Under the present synthesis conditions for the c-BN:Ce single crystals, the chemical potentials are unknown. Therefore, we adopt a general approach in which the chemical potentials are treated as variables. μ_B and μ_N are considered to range between the following extreme conditions: (a) the B-rich limit described as $\mu_B = \mu_{B(bulk)}$ and $\mu_N = 1/2\mu_{N_2} + \Delta H_f$ (ΔH_f, the theoretical formation energy of c-BN, is -2.69 eV) and (b) the N-rich limit described as $\mu_B = \mu_{B(bulk)} + \Delta H_f$ and $\mu_N = \frac{1}{2}\mu_{N_2}$. μ_{Ce} is given via the additional condition of $\mu_{Ce} + \mu_N = \mu_{CeN(bulk)}$, corresponding to the solubility limit of Ce determined by the segregation of CeN.

As expected from the huge size mismatch, the formation energies of Ce simply substituted for the B and N sites (Ce_B and Ce_N) are tremendously high for any charge state

[Figs. 3(a) and 3(b)]. On the other hand, if we consider vacancies at the nearest neighbor sites of Ce_B and Ce_N [Ce_B-$4V_N$ and Ce_N-mV_B ($m = 1$–4)], the formation energies are reduced under most conditions of the chemical potentials and Fermi level. In particular, point-defect structures $(Ce_N$-$4V_B)^q$, where the superscript q denotes the charge state of the defect complex, show very low or negative formation energies at a high Fermi level for $q = -6$ at the B-rich limit [Fig. 3(a)] and for $q = -5$ and -6 at the N-rich limit [Fig. 3(b)]. The Ce_N-$4V_B$ complex is energetically preferable to isolated defects also in view of the binding energy; for instance, when the Fermi level is at the conduction band minimum, the binding energy relative to Ce_N and $4V_B$ is 20.1 eV. The analysis of the one-electron structure and charge distribution suggests that the valence state of Ce in $(Ce_N$-$4V_B)^{6-}$ is 3+, while it is 4+ for $(Ce_N$-$4V_B)^{5-}$. On the basis of the EELS
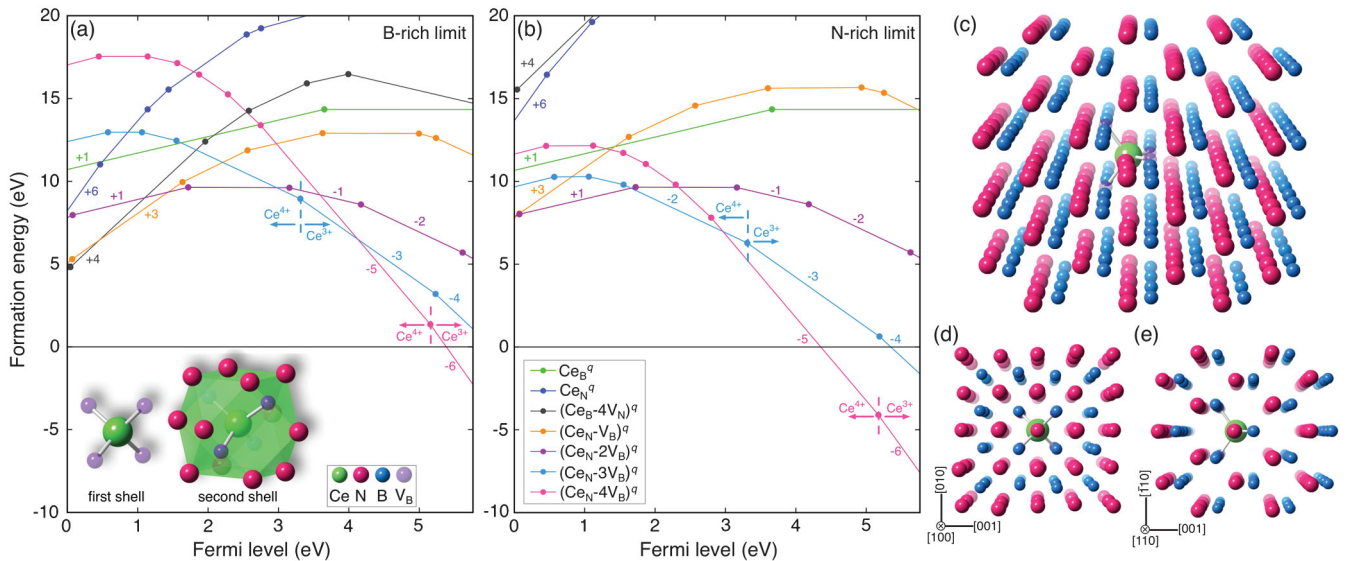
FIG. 3 (color).   Formation energies of Ce_B^q, Ce_N^q, $(Ce_B$-$4V_N)^q$, and $(Ce_N$-$mV_B)^q$ ($m = 1$–4) as a function of the Fermi level under two extreme chemical potential conditions: (a) the B-rich limit and (b) the N-rich limit. The range of the Fermi level is given by the valence band maximum (0 eV) and the conduction band minimum (5.8 eV). The slope corresponds to the charge state ($q = -6$–$+6$). (c) Relaxed $(Ce_N$-$4V_B)^{6-}$ complex point-defect structure and (d) its [100] and (e) [110] views. The first (V_B-tetrahedron) and second shells of the $(Ce_N$-$4V_B)^{6-}$ structure model are shown in the inset of (a). A small amount of relaxation in the second shell of N atoms is evident in (c).

result that the valence state of Ce is $3+$, we conclude that the experimentally observed configuration must be $(Ce_N$-$4V_B)^{6-}$.

As shown in Fig. 3(a) (inset), the N site in c-BN is surrounded by a boron-tetrahedron (first shell) and 12 N atoms (second shell). In the $(Ce_N$-$4V_B)^{6-}$ complex point-defect structure, not only are all the nearest B sites vacant but also the second shell, consisting of N atoms, exhibits a small structural relaxation. The local Ce structure is isotropic and the Ce atom is located at the N site without any displacement. These features are evidently seen by the two projections of the relaxed structure shown in Figs. 3(d) and 3(e). The bond length of B-N in c-BN is 1.57 Å [27] (the present theoretical value is 1.56 Å), while that of Ce-N in $(Ce_N$-$4V_B)^{6-}$ is 2.62 Å (theoretical). This value is close to the Ce-N bond length in the compound CeN (2.5 Å), and hence the c-BN lattice can accommodate Ce dopant atoms, overcoming the huge atomic size mismatch. Using the $(Ce_N$-$4V_B)^{6-}$ complex point-defect structure model with a Ce atom at the N site and rather small atomic relaxation in its vicinity, our experimental images can be well matched by simulation, as already shown in Fig. 2(b) (inset).

Our findings indicate that even dopant atoms with extremely large size mismatch can be stably incorporated into host crystal lattices through the formation of complex point-defect structures. These results provide an alternative strategy for doping foreign atoms into crystals. By optimizing the condition for the formation of complex point-defect structures, we may be able to dope a wide variety of foreign atoms that would otherwise be insoluble into given crystalline host lattices, thereby enabling us to control unique functionalities in largely mismatched systems.

---

*Corresponding author.
ikuhara@sigma.t.u-tokyo.ac.jp

[1] R. H. Wentorf, R. C. DeVries, and F. P. Bundy, Science **208**, 873 (1980).
[2] G. Blasse and B. G. Grabmaier, *Luminescent Materials* (Springer, Berlin, 1994).
[3] O. Mishima, J. Tanaka, S. Yamaoka, and O. Fukunaga, Science **238**, 181 (1987).
[4] O. Mishima and K. Era, in *Electric Refractory Materials*, edited by Y. Kumashiro (Marcel Dekker, New York, 2000), p. 495.

[5] T. Taniguchi, K. Watanabe, S. Koizumi, I. Sakaguchi, T. Sekiguchi, and S. Yamaoka, Appl. Phys. Lett. **81**, 4145 (2002).

[6] J. Wentorf and R. H. Wentorf, J. Chem. Phys. **36**, 1990 (1962).

[7] U. Vetter, H. Hofsass, and T. Taniguchi, Appl. Phys. Lett. **84**, 4286 (2004).

[8] A. Nakayama, T. Taniguchi, Y. Kubota, K. Watanabe, S. Hishita, and H. Kanda, Appl. Phys. Lett. **87**, 211913 (2005).

[9] T. Taniguchi and K. Watanabe, J. Cryst. Growth **303**, 525 (2007).

[10] S. J. Pennycook and L. A. Boatner, Nature (London) **336**, 565 (1988).

[11] K. Nakamura, H. Kakibayashi, K. Kanehori, and N. Tanaka, J. Electron Microsc. **46**, 33 (1997).

[12] M. Varela, S. D. Findlay, A. R. Lupini, H. M. Christen, A. Y. Borisevich, N. Dellby, O. L. Krivanek, P. D. Nellist, M. P. Oxley, L. J. Allen, and S. J. Pennycook, Phys. Rev. Lett. **92**, 095502 (2004).

[13] P. M. Voyles, D. A. Muller, J. L. Grazul, P. H. Citrin, and H.-J. L. Gossmann, Nature (London) **416**, 826 (2002).

[14] A. Y. Borisevich, A. R. Lupini, and S. J. Pennycook, Proc. Natl. Acad. Sci. U.S.A. **103**, 3044 (2006).

[15] N. Shibata, S. D. Findlay, S. Azuma, T. Mizoguchi, T. Yamamoto, and Y. Ikuhara, Nat. Mater. **8**, 654 (2009).

[16] See Supplemental Material at http://link.aps.org/supplemental/10.1103/PhysRevLett.110.065504 for evaluation of Ce concentration, first-principles calculations, and ADF STEM image simulations.

[17] P. A. Crozier, R. Wang, and R. Sharma, Ultramicroscopy **108**, 1432 (2008).

[18] J. A. Fortner and E. C. Buck, Appl. Phys. Lett. **68**, 3817 (1996).

[19] P. J. Hay, R. L. Martin, J. Uddin, and G. E. Scuseria, J. Chem. Phys. **125**, 034712 (2006).

[20] J. L. F. Da Silva, M. V. Ganduglia-Pirovano, J. Sauer, V. Bayer, and G. Kresse, Phys. Rev. B **75**, 045121 (2007).

[21] F. Oba, A. Togo, I. Tanaka, J. Paier, and G. Kresse, Phys. Rev. B **77**, 245202 (2008).

[22] F. Oba, A. Togo, I. Tanaka, K. Watanabe, and T. Taniguchi, Phys. Rev. B **81**, 075125 (2010).

[23] P. E. Blöchl, Phys. Rev. B **50**, 17953 (1994).

[24] A. V. Krukau, O. A. Vydrov, A. F. Izmaylov, and G. E. Scuseria, J. Chem. Phys. **125**, 224106 (2006).

[25] J. Paier, M. Marsman, K. Hummer, G. Kresse, I. C. Gerber, and J. G. Angyan, J. Chem. Phys. **124**, 154709 (2006).

[26] S. Lany and A. Zunger, Modelling Simul. Mater. Sci. Eng. **17**, 084002 (2009).

[27] E. Knittle, R. M. Wentzcovitch, R. Jeanloz, and M. L. Cohen, Nature (London) **337**, 349 (1989).

[28] R. F. Egerton, *Electron Energy-Loss Spectroscopy in the Electron Microscope* (Plenum, New York, 1996).